nature materials

Article

https://doi.org/10.1038/s41563-024-01884-2

Heat-resistant super-dispersed oxide strengthened aluminium alloys

In the format provided by the authors and unedited

Table of Contents

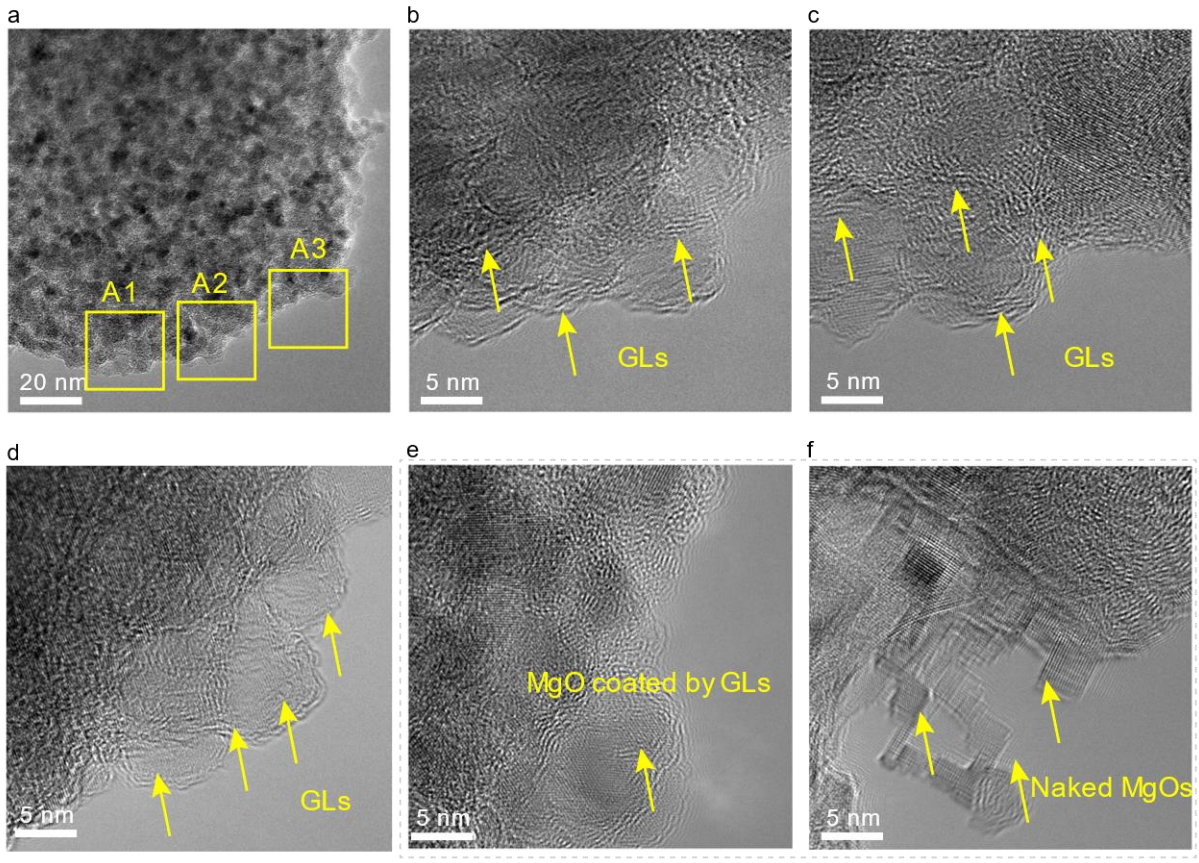

Supplementary Fig. 1| The MgO NPs coated by GL layers. a, TEM image of MgO@GL showing the MgO particles with a size of ~5 nm coated by GL layers. **b-d**, High resolution TEM images of MgO@GL corresponding the areas A1, A2 and A3, respectively in **a**. These images demonstrate that the surface of MgO particles is coated with 2-3 layers of GL nanosheets. **e**, **f**, TEM images of MgO particles coated with GL layers before electron-beam irradiation and exposed MgO particles after electron-beam irradiation, respectively.

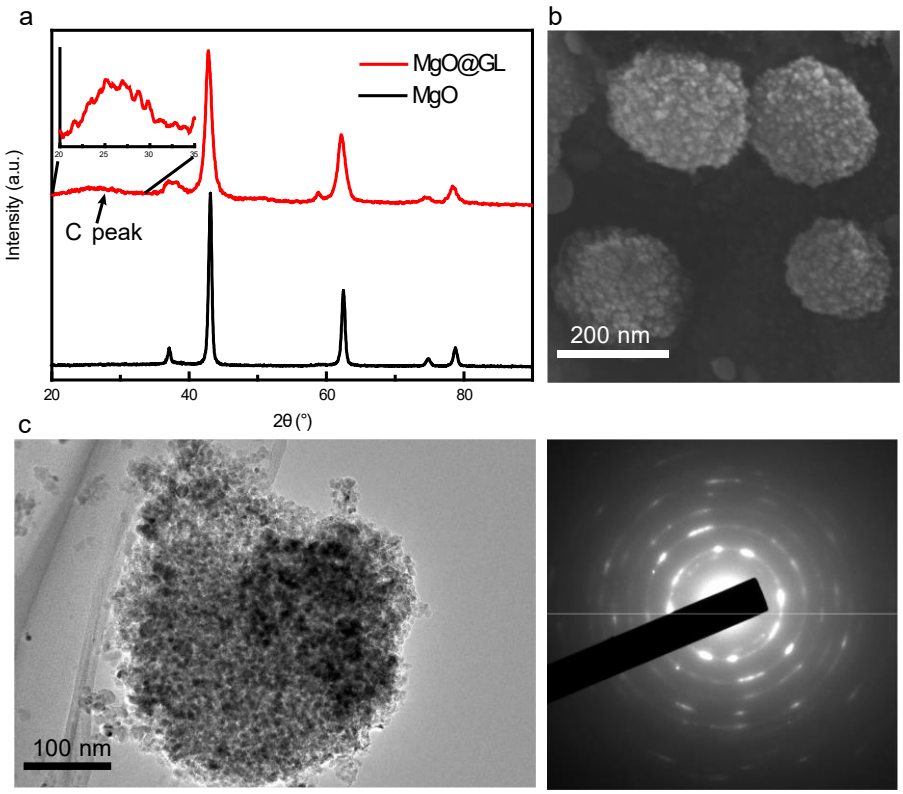

Supplementary Fig. 2| Microstructural characterizations of MgO@GL. a, XRD patterns of initial MgO@GL and commercial MgO NPs. **b**, **c**, SEM and TEM images of MgO@GL showing a pomegranate-like architecture of MgO particles with a size of ~5 nm.

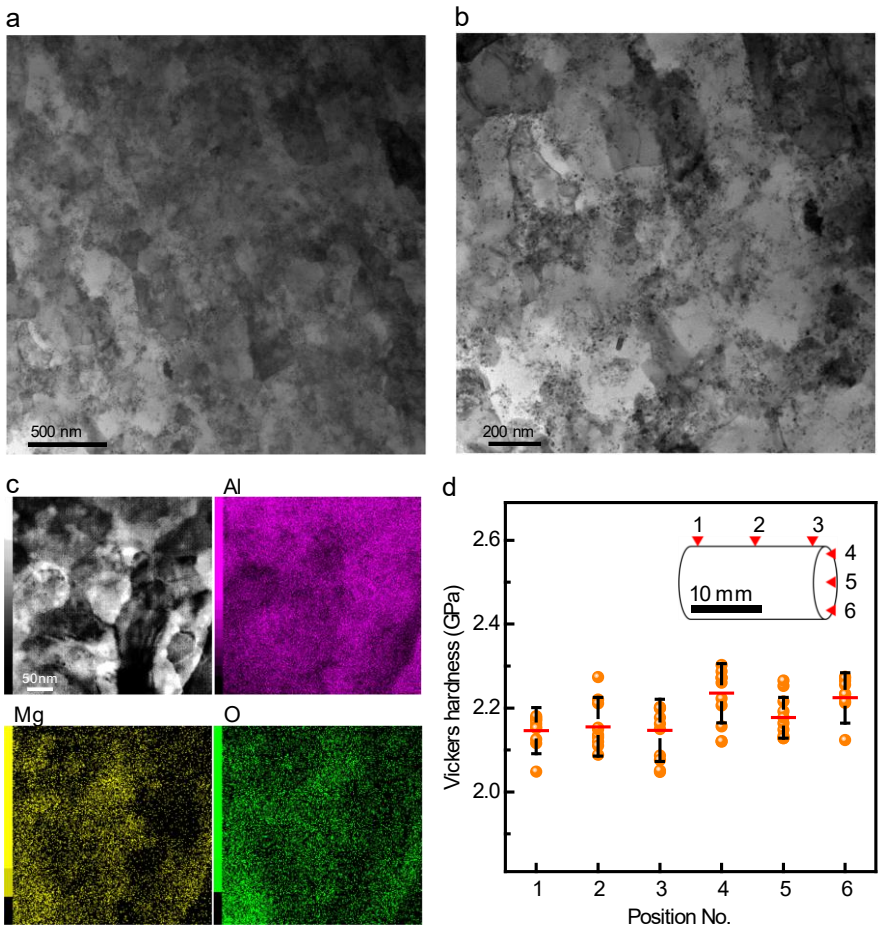

Supplementary Fig. 3| Uniform distribution of MgO NPs across the whole composites. a, **b**, Bright-field TEM images of the as-extruded MgO@GL/Al presenting the dispersed MgO NPs in the Al matrix. **c**, X-ray energy dispersive spectroscopy (XEDS) mapping displaying the distribution of Al, Mg and O elements of the sample. **d**, Distribution of Vickers microhardness (orange dots) at different positions in the sample (as shown in the inset). The red bar is the average of 10 measurements, and the error bars are the standard deviation of the mean.

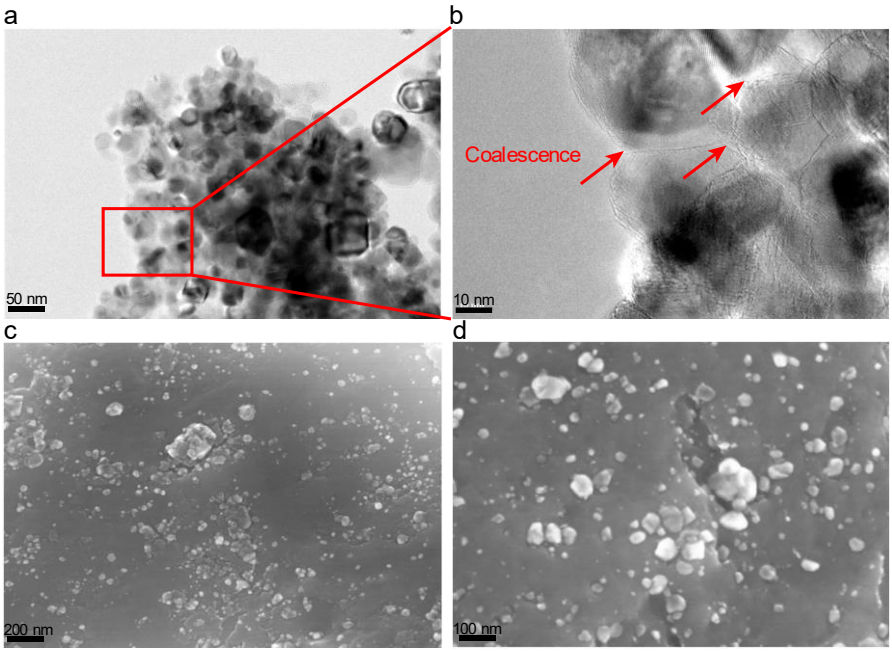

Supplementary Fig. 4| Agglomeration of the commercial MgO NPs. a, **b** TEM images of commercial MgO NPs indicating the coalescence between particles. **c**, **d** SEM images of the cross-section of MgO/Al composites revealing the agglomeration and coalescence of the commercial MgO NPs in the composite.

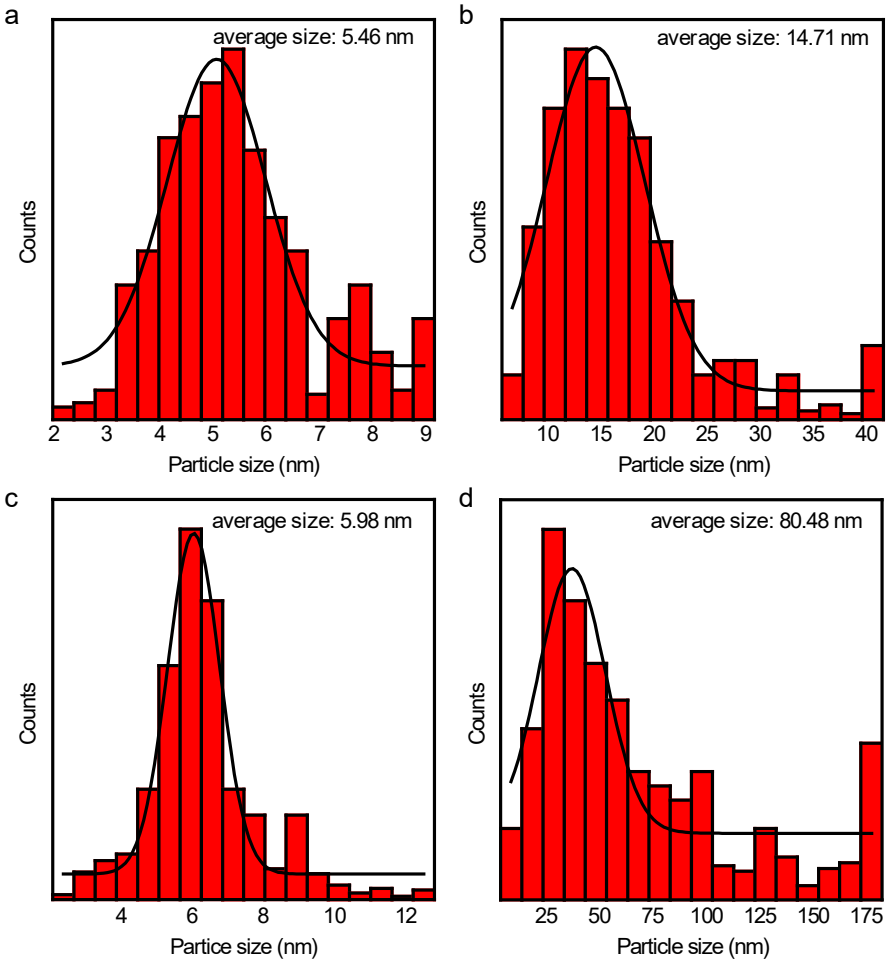

Supplementary Fig. 5| The size distribution of MgO@GL and MgO NPs. a, **b**, The size statistical histograms of over 2000 particles of initial MgO@GL and commercial MgO NPs. **c**, **d**, The size statistical histograms of MgO NPs in MgO@GL/Al and MgO/Al composites, respectively.

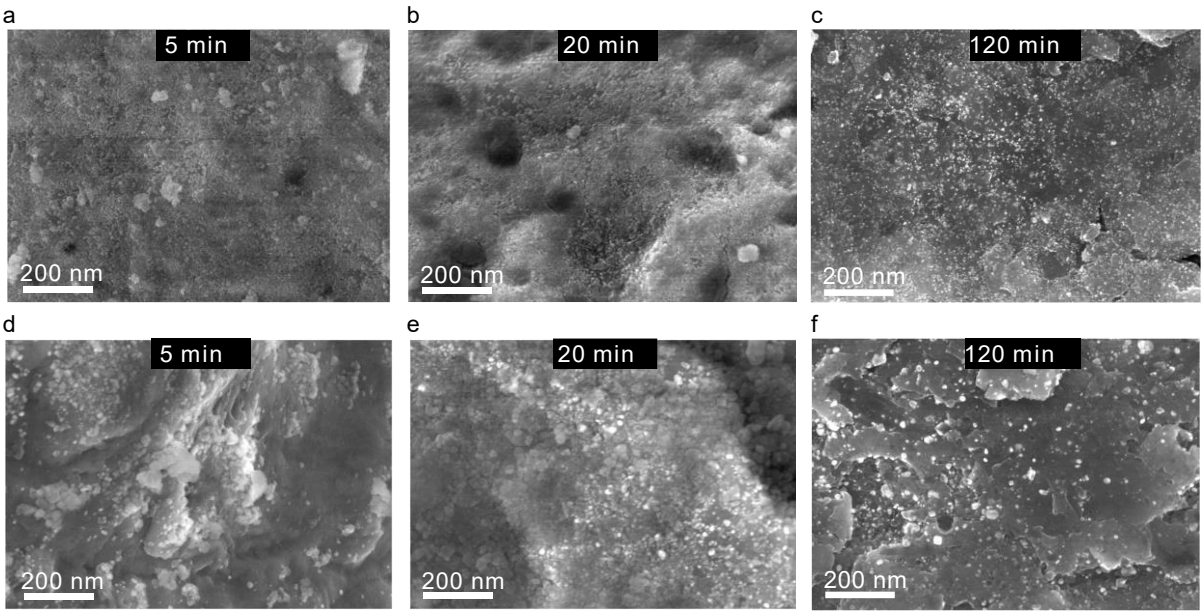

Supplementary Fig. 6| Dispersion states of particles at different milling times. a-c, SEM images of dispersion of MgO@GL in Al powder after milling for 5 minutes, 20 minutes and 120 minutes, respectively. **d-f**, SEM images of dispersion of commercial MgO NPs in Al powder after milling for 5 minutes, 20 minutes and 120 minutes, respectively.

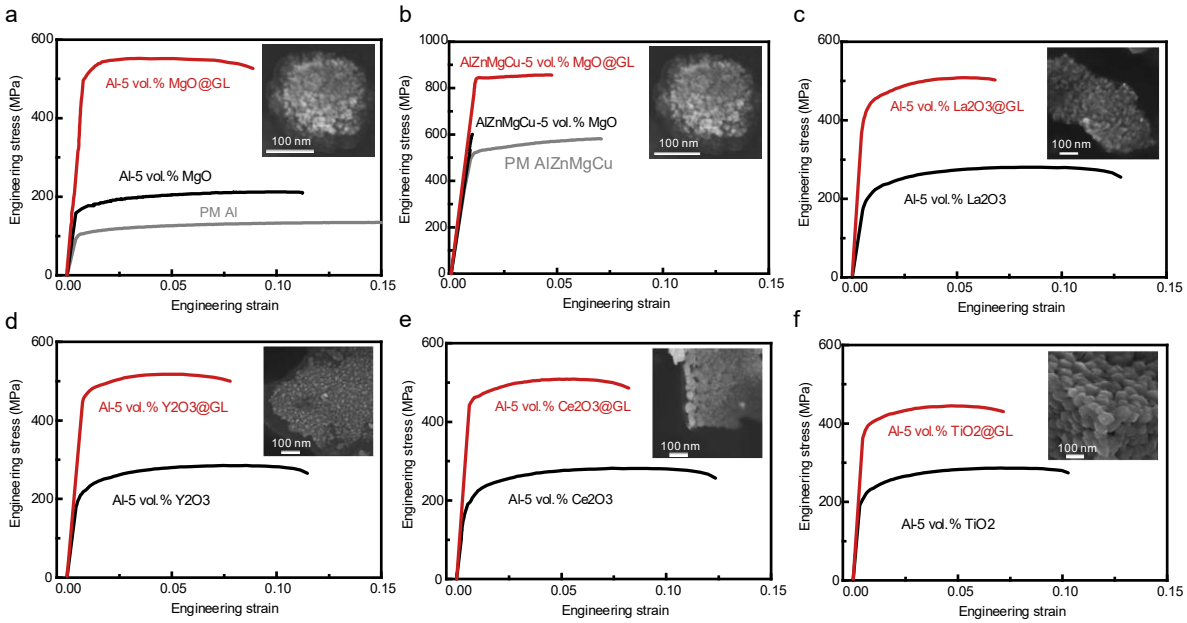

Supplementary Fig. 7| The tensile engineering stress-strain curves of the ODS Al bulk materials.

a, Al-5 vol.% MgO@GL. **b,** AlZnMgCu-5 vol.% MgO@GL. **c,** Al-5 vol.% La_2O_3@GL. **d,** Al-5 vol.% Y_2O_3. **e,** Al-5 vol.% Ce_2O_3@GL. **f**, Al-5 vol.% TiO_2@GL.

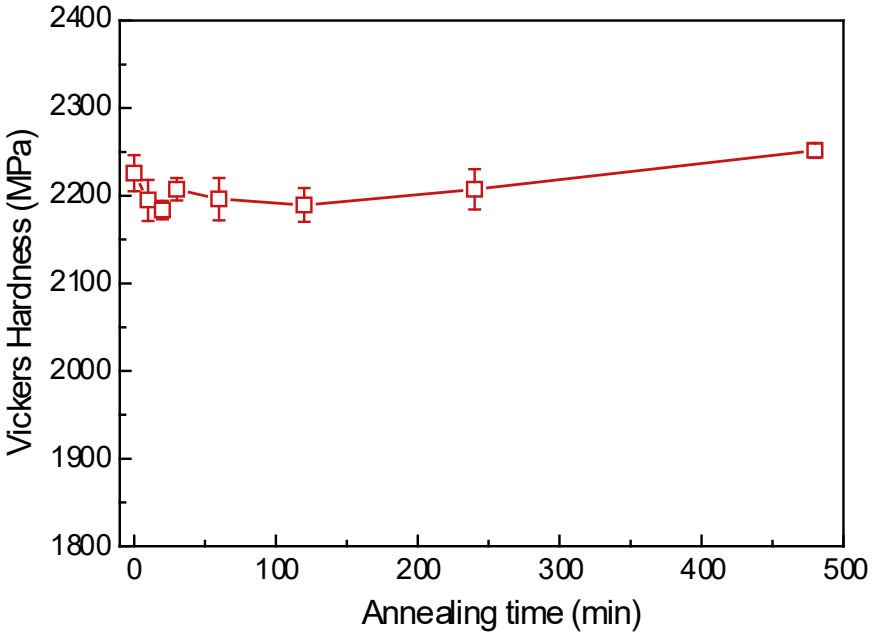

Supplementary Fig. 8| Vickers hardness of the MgO@GL/Al versus annealing time at 600°C.

Each data point is the average of three measurements and the error bars are the standard deviation of the mean.

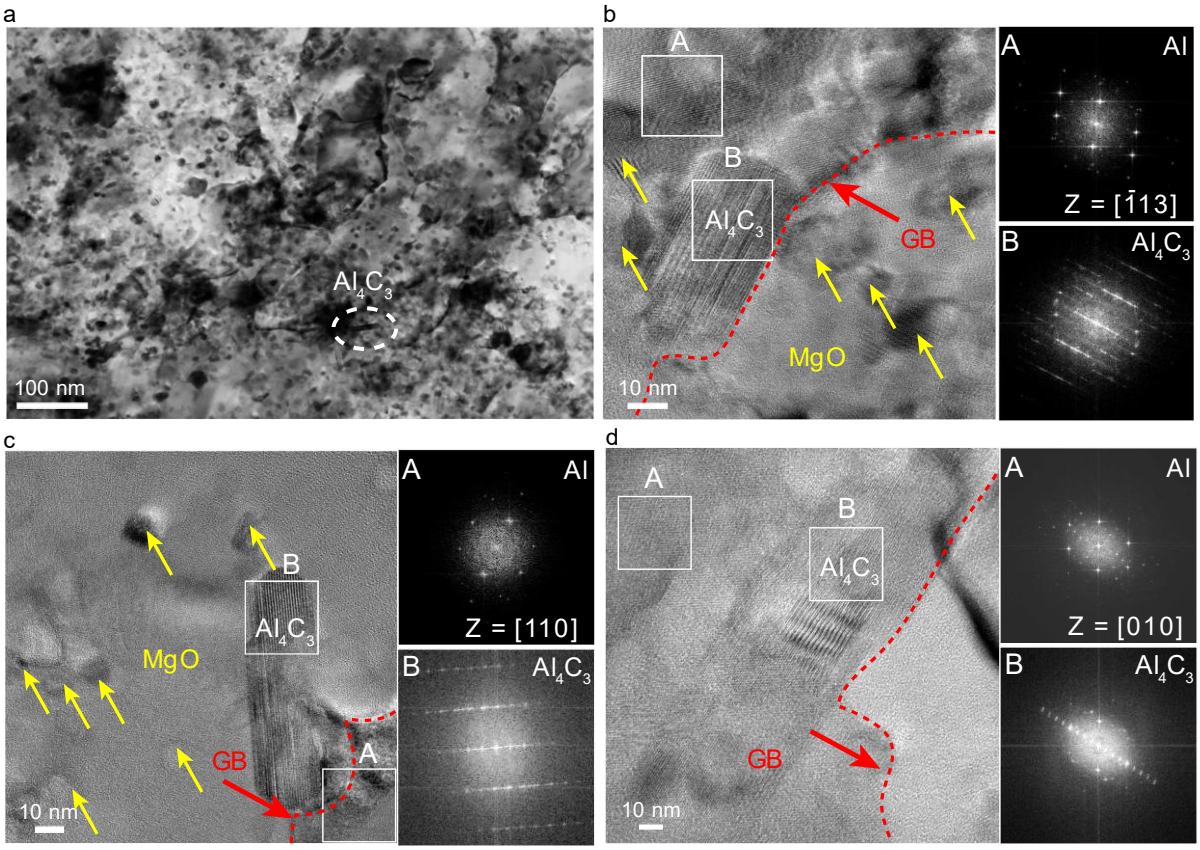

Supplementary Fig. 9| Distribution of carbon elements. **a**, Bright-field STEM image of the as-extruded MgO@GL/Al. The white dashed line displays a small amount of Al_4C_3. **b**, **c**, HRTEM images of the MgO@GL/Al bulks after sintering (**b**) and extrusion (**c**) showing the Al_4C_3 at GBs. Insets are the FFT patterns of corresponding area. **d**, HRTEM images of the GL/Al (the GL were from the MgO@GL after etching MgO by HCl) bulk presenting the Al_4C_3 at GBs. Insets are the FFT patterns of corresponding area.

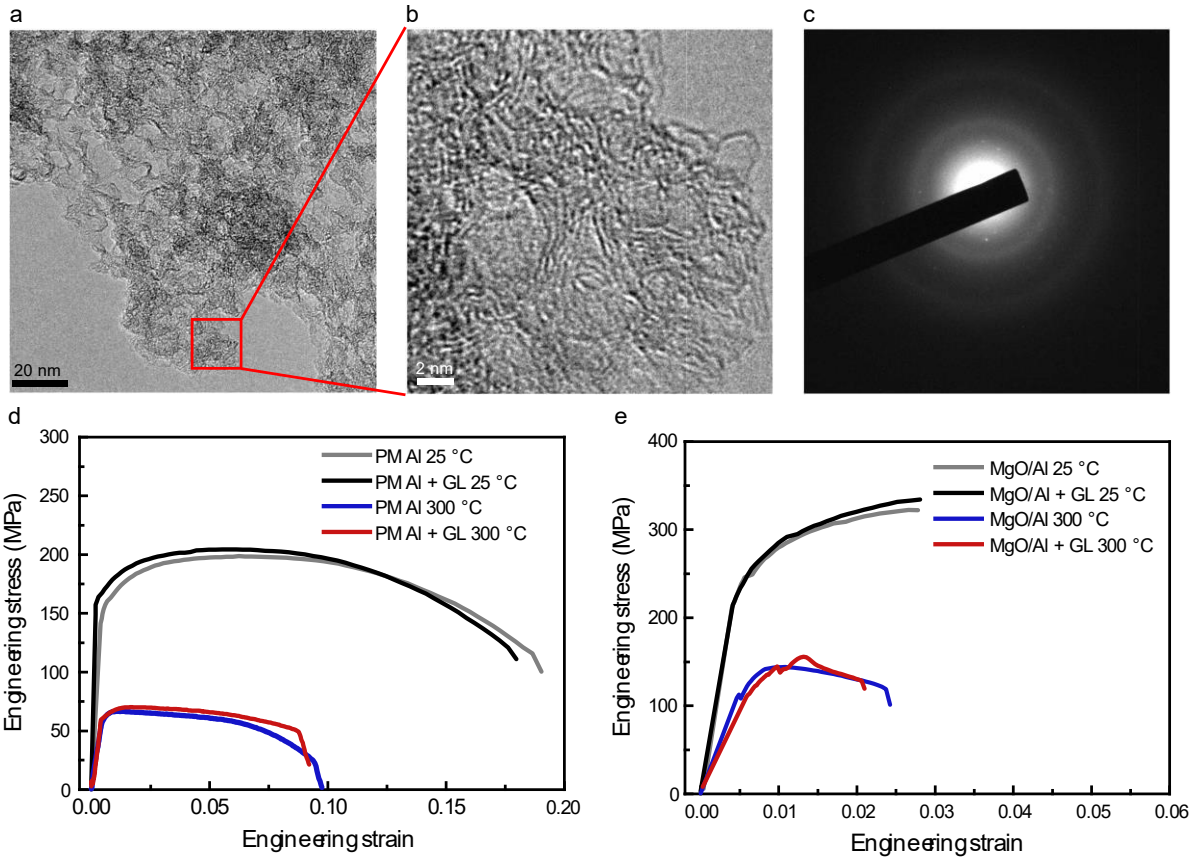

Supplementary Fig. 10| Negligible influence of carbon in MgO@GL on the mechanical properties of alloys. a, **b**, TEM images of GL coatings in the MgO@GL after etching MgO by HCl. **c**, Diffraction pattern from the area of **a** corresponding to the GL coatings. **d**, Tensile engineering stress-strain curves of the as-extruded PM Al and PM Al + GL at 25°C/300°C. **e**, Tensile engineering stress-strain curves of the as-extruded MgO/Al and MgO/Al + GL at 25°C/300°C. The corresponding GL content in MgO@GL/Al separated from MgO@GL was added to the PM Al and MgO/Al, and the samples of PM Al + GL and MgO/Al + GL were fabricated by the same process.

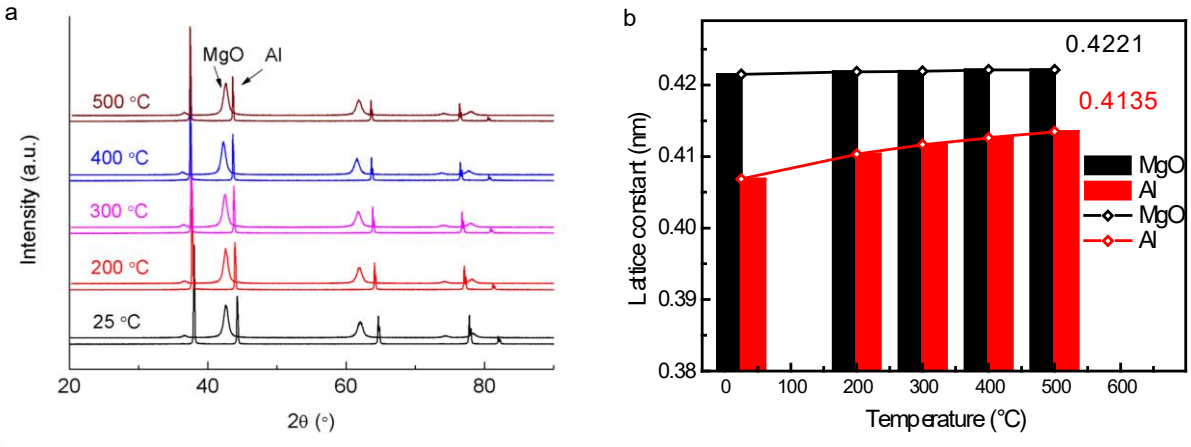

Supplementary Fig. 11| Lattice constants of Al and MgO obtained by high temperature XRD. a, In-situ HT-XRD patterns of MgO and Al at different temperatures. **b,** Comparative bar chart of the lattice constants of MgO and Al at different temperatures.

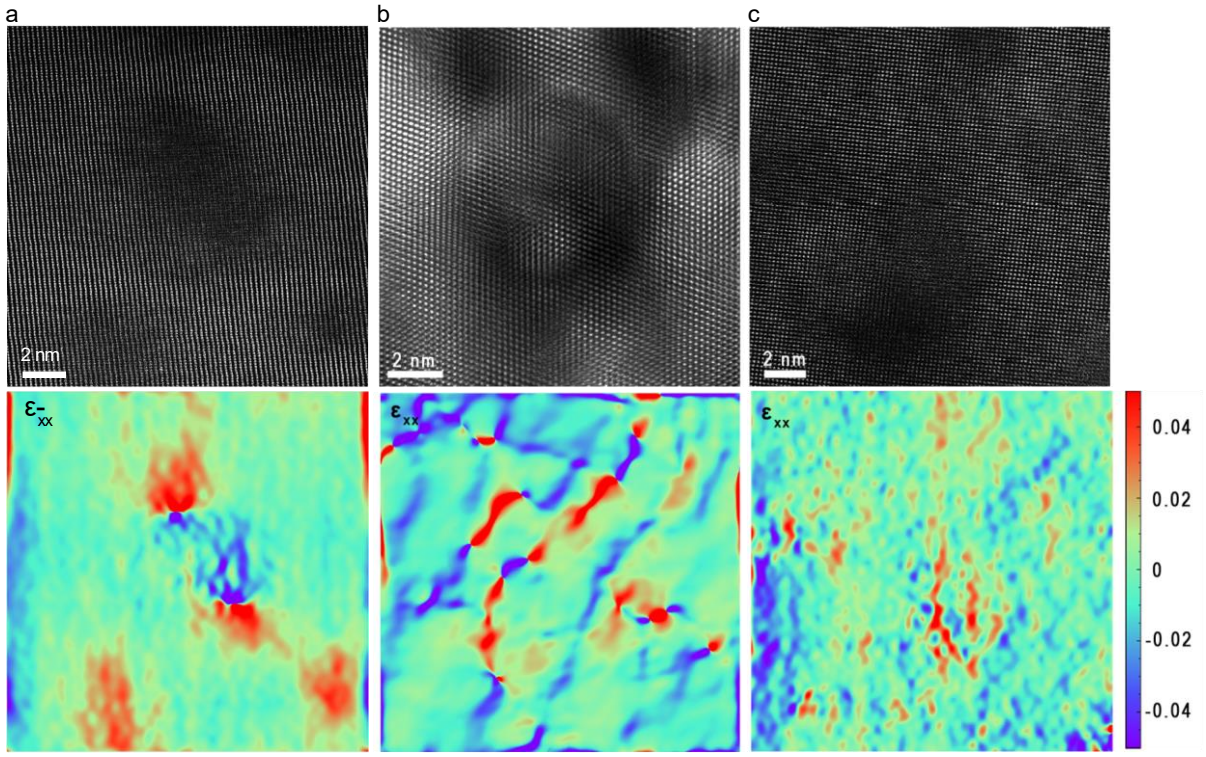

Supplementary Fig. 12| Interface structure and strain distribution. a-c, Atomic-resolution HAADF STEM images and in-plane (ε_{xx}) strain field maps obtained by GPA of the HAADF STEM image taken from <112>(**a**), <110>(**b**) and <010>(**c**) zone axes, showing the minimized lattice strain around coherent MgO NPs.

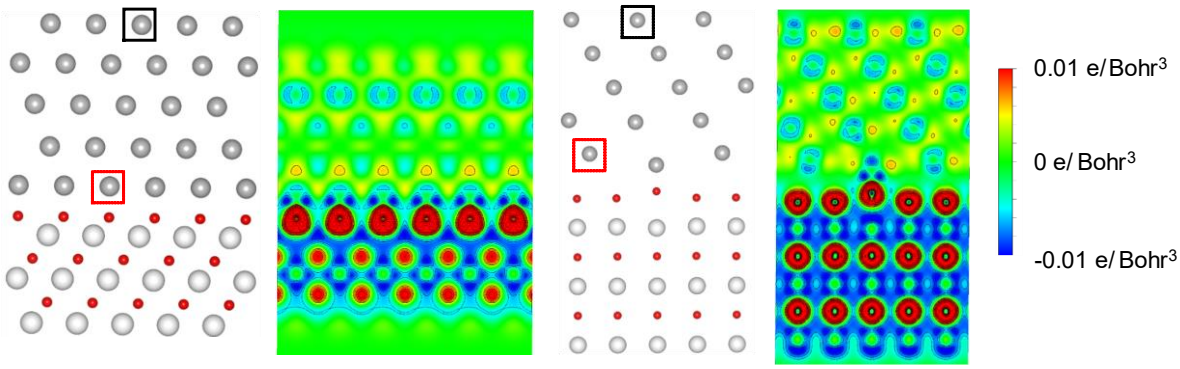

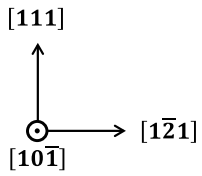

E (J/m^2)	Adsorption energy	Vacancy formation energy		a-b
		Interface (a)	Matrix (b)	
$Al_{(111)}/MgO_{(111)}$	7.96	2.28	0.82	1.46
$Al_{(111)}/MgO_{(100)}$	0.22	0.76	0.97	-0.21
$Al_{(111)}$	1.67		0.97	

Supplementary Fig. 13| DFT calculations of vacancy formation energies and binding energies.

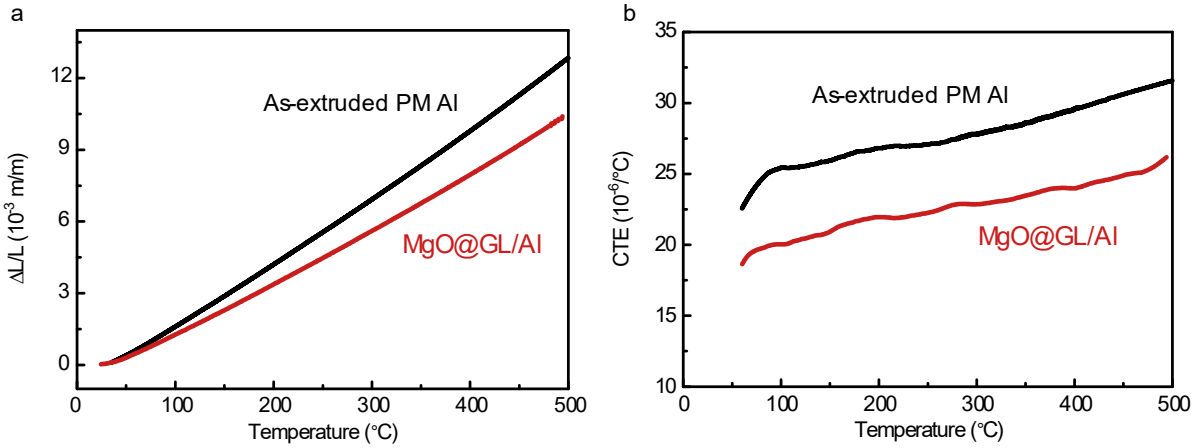

Supplementary Fig. 14| Thermal expansion behaviours of the as-extruded PM Al and MgO@GL/Al. a, The relative length of the as-extruded PM Al and MgO@GL/Al changes with temperature. **b**, CTE curves of the as-extruded MgO@GL/Al versus temperature compared with the as-extruded PM Al samples.

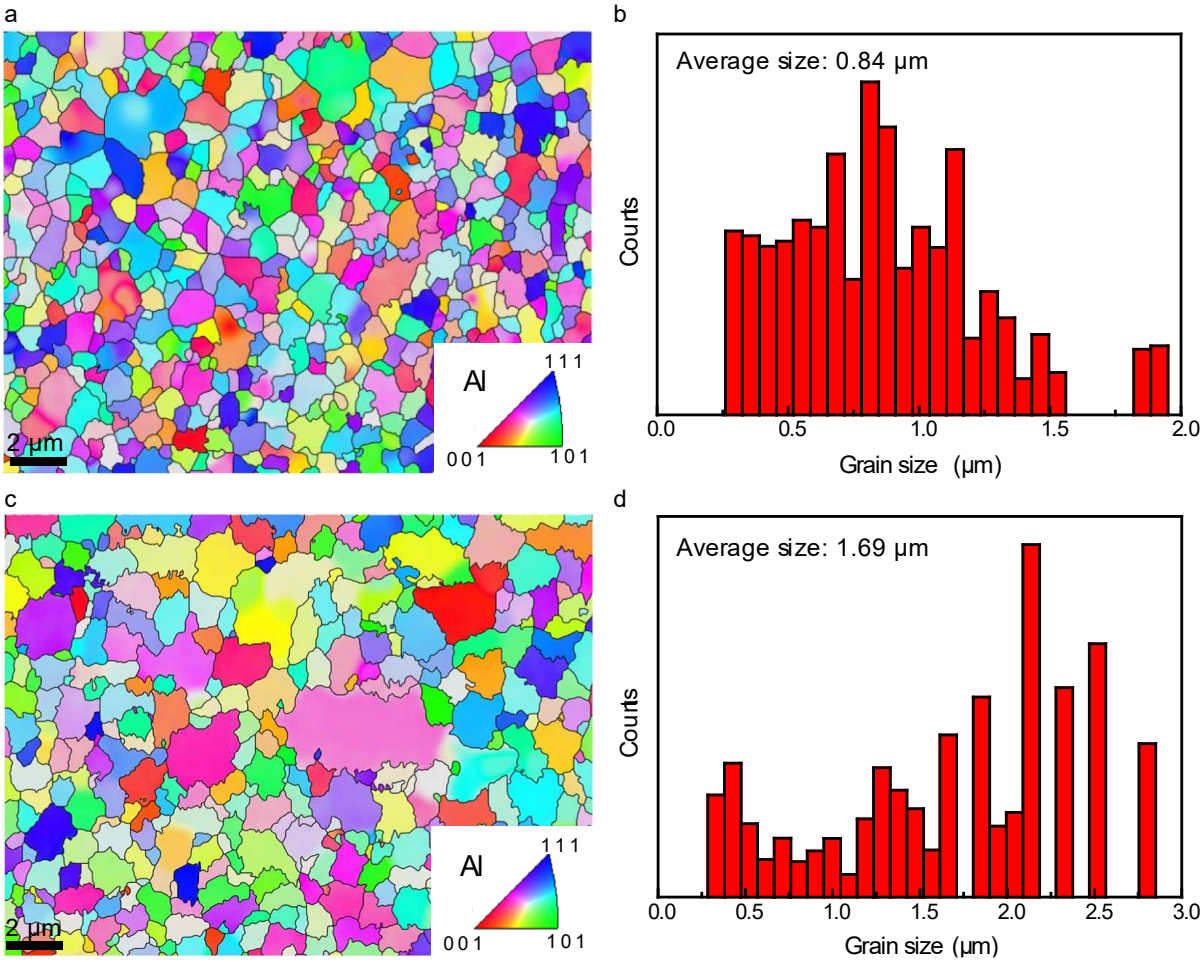

Supplementary Fig. 15| Grain coarsening of the PM Al. a, c, Typical cross-sectional EBSD grain maps of the PM Al sample before **(a)** and after **(c)** 8 h annealing at 600°C showing that grain size obviously coarsened. **b, d,** Histograms indicating the corresponding grain size distributions.

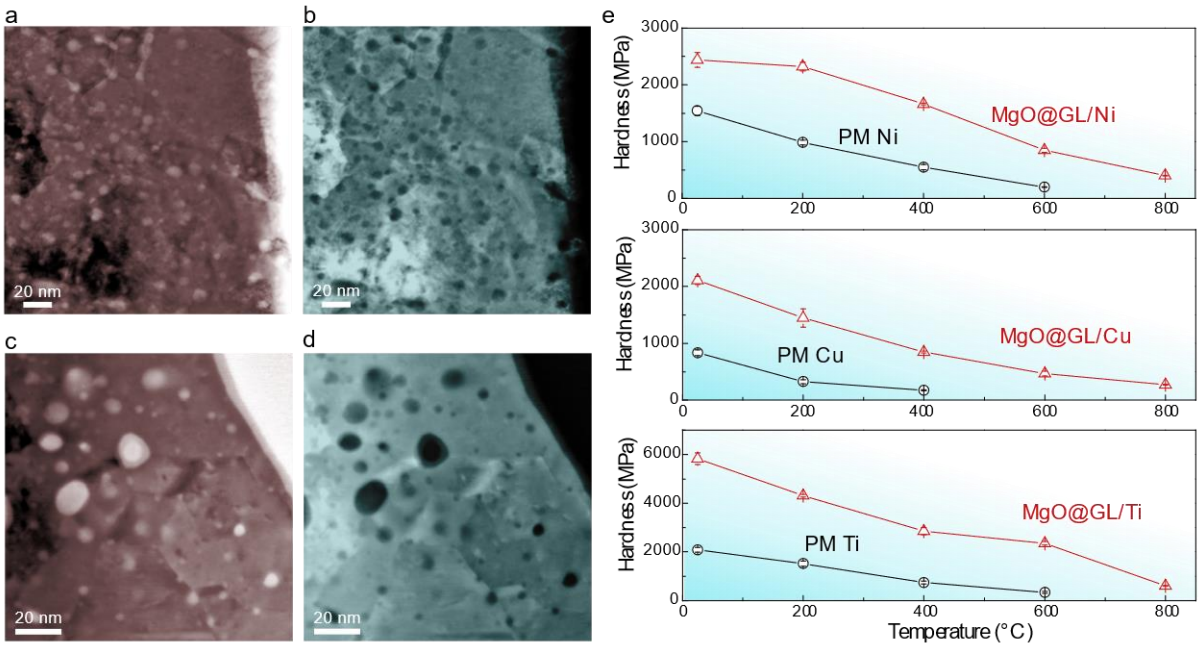

Supplementary Fig. 16| Microstructure of ODS Ni and Cu alloys with 5.0 vol.% MgO@GL particles and high-temperature Vickers hardness of PM Ni, Cu, Ti and corresponding ODS alloys with 5.0 vol.% MgO@GL particles. a, b, BF-STEM and the corresponding DF-STEM images of ODS Ni alloy demonstrating the uniform dispersion of MgO NPs. **c, d,** BF-STEM and the corresponding DF-STEM images of ODS Cu alloy showing the uniform dispersion of MgO NPs. **e**, Vickers hardness of MgO@GL/Ti, MgO@GL/Cu, MgO@GL/Ni versus temperature compared with PM Ti, PM Cu and PM Ni samples, respectively. Each data point is the average of five measurements and the error bars are the standard deviation of the mean.

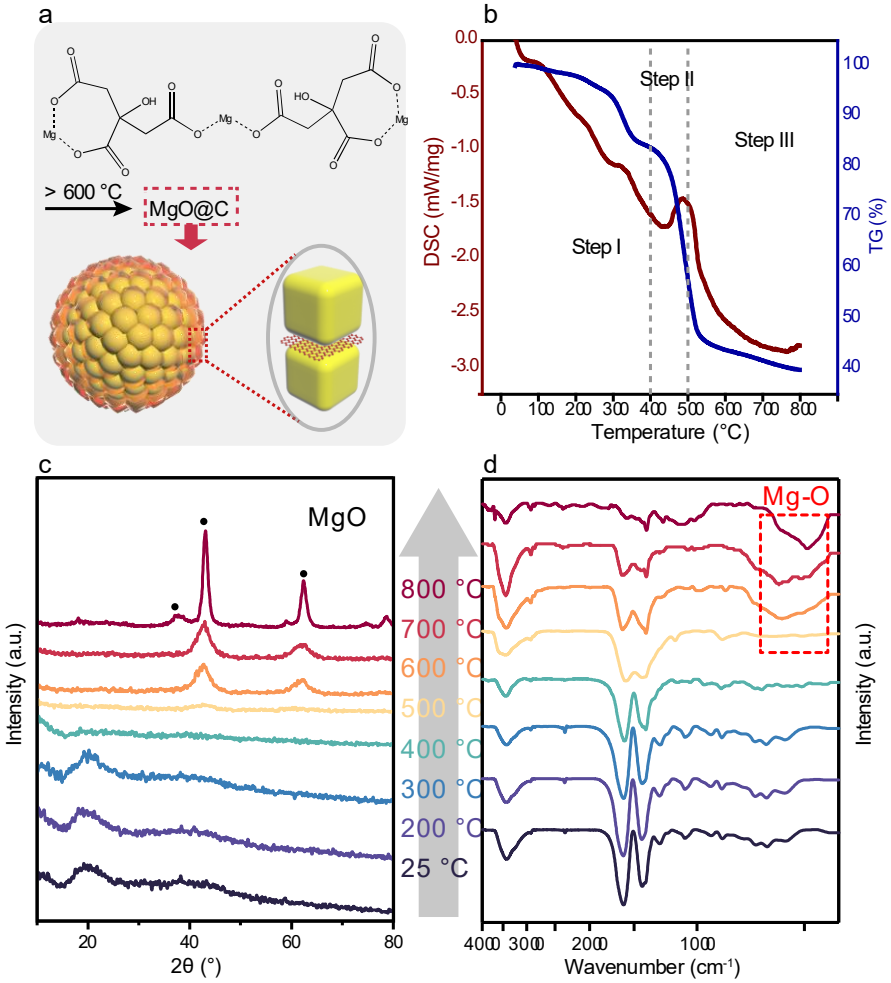

Supplementary Fig. 17| Synthesis of MgO@GL. a, Schematic illustration of the vacuum pyrolysis of magnesium citrate precursor. **b**, DSC and TGA curves of magnesium citrate heated from room temperature to 800°C. **c**, **d**, In-situ HT-XRD patterns and HT-FTIR spectra of magnesium citrate at different temperatures.

Supplementary Table 1| The summarized reported data on the number density of dispersed phases in various common Al alloys and ODS metals.

Materials	Dispersed phases	Number density (m^{-3})	Reference
Al-3.5Cu	θ'	~2×10^{20}	1
Al-3.5Cu	θ	~9×10^{18}	1
Al-Zn-Mg-Cu	T'	4.43×10^{22}	2
Al-Zn-Mg-Cu	T' and η'	0.9-7.48×10^{23}	2
Al-Mg-Si-Mn	β' and β''	0.003-1.38×10^{21}	3
Fe-Cr-W-Ti-Y_2O_3	Y_2O_3	0.1-7×10^{23}	4
Fe-Ti-Zr-O	ZrO	0.3-1.3×10^{23}	5
Ni-Al-Cr-Fe-Ti-Y_2O_3	Y_2O_3	~8×10^{22}	6

Supplementary Table 2| Crystal type and Lattice constant of potential oxides for ODS Al.

	Crystal lattice type	Lattice constant
Al	**Cubic**	**a ≈ 0.405 nm**
MgO	**Cubic**	**a ≈ 0.420 nm**
γ-Al_2O_3	Cubic	a ≈ 0.799 nm
α-Al_2O_3	Hexagonal	a ≈ 0.476 nm, c ≈ 1.299 nm
TiO_2	Tetragonal	a ≈ 0.378 nm, c ≈ 0.951 nm
La_2O_3	Hexagonal	a ≈ 0.546 nm, c ≈ 1.322 nm
Y_2O_3	Cubic	a ≈ 1.060 nm
Ce_2O_3	Hexagonal	a ≈ 0.542 nm, c ≈ 1.327 nm

Supplementary Note 1. Synthesis of MgO@GL.

Schematic synthesis process of the MgO@GL is illustrated in Supplementary Fig. 17a. The NPs with GL coatings were obtained through directly vacuum heating magnesium citrate ($Mg_3(C_6H_5O_7)_2 \cdot 9H_2O$) at 800°C. Referring to the decomposition of relevant citrate salts, this process involves the decomposition of the metal center and the carbonization of the ligands. Accordingly, the differential scanning calorimeter (DSC) and thermogravimetric analysis (TGA) curves of magnesium citrate show the obvious thermal reaction and weight loss steps (Supplementary Fig. 17b). The entire process is completed through several overlapping endothermic steps, except for an exothermic peak at 500°C, which corresponds to the formation of MgO nanocrystals. Two obvious weight loss steps are attributed to the loss of crystalline water (< 300°C), and the ligand transformation into carbon. In order to better understand the formation mechanism of MgO@GL during annealing, in situ high-temperature X-ray diffraction (HT-XRD) and Fourier transform infrared (HT-FTIR) measurements were performed using the same heating program (Supplementary Fig. 17c, d). In the HT-XRD pattern, the characteristic peaks of MgO crystal started to appear above 500°C (Supplementary Fig. 17c), which is consistent with the HT-FTIR spectra (Supplementary Fig. 17d) where characteristic peaks of Mg-O bonding at 400-500 cm^{-1} were observed at the same temperature. Therefore, at high temperature, organic ligands of the magnesium citrate precursor were transformed into carbon framework, and the Mg center was transformed into MgO crystals (500°C). The initially formed carbon framework acts as a confining structure, limiting the congregated growth of MgO and consequently leading to the formation of nanocrystalline MgO particles.

Supplementary Note 2. "Input energy".

In a dispersion system, "input energy" acts on nanoparticles to provide an impact velocity, thereby enhancing their kinetic energy to overcome the surface energy for a higher Weber number. For instance, during a ball milling process, the impact velocity of nanoparticles can be increased by raising the rotation speed or ball-to-material ratio.

The "input energy" is defined to reflect the kinetic energy needed for a given particle to achieve a Weber number of 100. According to the definition of the Weber number (ratio of the kinetic energy to surface energy, $We = \rho d v^2/\gamma$, where ρ, d, v and γ represent the density, diameter, impact velocity and surface energy, respectively), the "input energy" (E_{input}) is expressed as $E_{input} = 100\gamma/\rho d$, which represents the square of the particle impact velocity (v), with the corresponding unit being $J\ kg^{-1}$.

It should be noted that the "input energy" is inversely proportional to the nanoparticle diameter, varying based on the surface energy of different type of particles. The difficulty of dispersion can be measured by the "input energy", and the relative value between the two reflects the relative difficulty of dispersion. Based on the DFT results, with the γ of MgO@GL and MgO being ~0.02 J m^{-2} and ~2.18 J m^{-2}, the "input energy" demonstrates a difference of 2 to 3 orders of magnitude, especially indicating that the smaller the particles, the greater the absolute difference in the required "input energy". Fig. 1g presents the relationship between input energy and particle size for MgO@GL and MgO.

Supplementary Note 3. Calculations of number density and the interface density.

For calculating the number density of particles and the interface density caused by these particles, we employed statistical data on the distribution of particles within bulk material (Supplementary Fig. 5c). The following represents the details of our specific computational process:

To enhance the accuracy of our calculations, instead of using a direct statistical average diameter, we employed numerical integration. This method allowed for a more precise determination of the particle number density (ρ_p) and interface density (ρ_{inter}) in the material. The specific formula is as follows:

$$\rho_p = \sum \frac{f_p}{V_i v_i} \tag{1}$$

$$\rho_{inter} = \sum \frac{f_p A_i v_i}{V_i} \tag{2}$$

where f_p is the volume fraction of MgO nanoparticles, $f_p = 0.08$, v_i, V_i and A_i are the frequency, volume and area of particles of corresponding sizes, respectively. $i = 1 - 18$, denotes the 18 boxes in the statistical histogram (Supplementary Fig. 5c). In our statistical approach, we implemented a conservative measurement technique. To be specific, the particle size we measured is the maximum width of the particles on the observed plane, and we approximated this size as the face diagonal of cubic particles. Therefore,

$$V_i = (\frac{r_i}{\sqrt{2}})^3 \tag{3}$$

$$A_i = 6(\frac{r_i}{\sqrt{2}})^2 \tag{4}$$

where r_i is the particle sizes corresponding to each of the 18 boxes. The calculated ρ_p and ρ_{inter} are ~9×10^{23} m^{-3} and ~1.4×10^{8} m^{-1}.

Supplementary Note 4. Fabrication of the ODS Ni, Cu and Ti alloys.

Pure metal (Ni, Cu, Ti) powders (average diameter: ~20.0 μm, Changsha Tianjiu Metal Materials, Co. Ltd., China) and 5.0 Vol% MgO@GL powders were loaded into a WC jar. The jar was filled with the milling media (WC balls) and the processing control agent (~1.0 wt.% steric acids) in an argon atmosphere inside a glove box. The ball-to-powder ratio was 20:1 by weight. The powders were then milled for 10 h at a rotation rate of 400 rpm to obtain composite powders. The milling process was conducted using a planetary ball mill at room temperature. To avoid excessive temperature increasing during milling, the grinding jar was fan-cooled, and 30 min interval was used during ball-milling. Hot vacuum degassed at temperatures up to 500°C for 4 h with a final pressure in the range 10^{-2} Pa. The vacuum hot pressing parameters of PM Cu and ODS Cu are 600°C and 150 MPa for 1 h. While sintering with parameters of 1000°C and 150 MPa for 1 h was carried out to obtain PM Ni, Ti and ODS Ni, Ti alloys.

Supplementary References:

1. Heugue, P., Larouche, D., Breton, F., Martinez, R. & Chen, X. G. Evaluation of the Growth Kinetics of θ′ and θ-Al_2Cu precipitates in a binary Al-3.5 Wt Pct Cu alloy. *Metall. Mater. Trans. A* **50**, 3048-3056 (2019).
2. Zou, Y. et al. Investigation on microstructure and mechanical properties of Al-Zn-Mg-Cu alloys with various Zn/Mg ratios. *J. Mater. Sci. Technol.* **85**, 106-113 (2021).
3. Rakhmonov, J., Liu, K., Rometsch, P., Parson, N. & Chen, X. Effects of Al (MnFe) Si dispersoids with different sizes and number densities on microstructure and ambient/elevated-temperature mechanical properties of extruded Al–Mg–Si AA6082 alloys with varying Mn content. *J. Alloy Compd*. **861**, 157937 (2021).
4. Miller, M. K., Russell, K. F. & Hoelzer, D. T. Characterization of precipitates in MA/ODS ferritic alloys. *J. Nucl. Mater.* **351**, 261-267 (2006).
5. Darling, K. A. et al. Structure and mechanical properties of Fe–Ni–Zr oxide-dispersion-strengthened (ODS) alloys. *J. Nucl. Mater.* **467**, 205-211 (2015).
6. Oono, N., Ukai, S., Kondo, S., Hashitomi, O. & Kimura, A. Irradiation effects in oxide dispersion strengthened (ODS) Ni-base alloys for Gen. IV nuclear reactors. *J. Nucl. Mater.* **465**, 835-841 (2015).